Mixed Planewave and Localized Orbital Basis for Sparse-Stochastic Hybrid TDDFT

Kyle Chen, Barry Y. Li, Tucker Allen, and Daniel Neuhauser*
Department of Chemistry and Biochemistry, University of California, Los Angeles, Los Angeles, CA, 90095, USA
(Dated: June 24, 2025)

We present a mixed basis-set approach to obtain optical absorption spectra within a generalized Kohn-Sham time-dependent density functional theory framework. All occupied valence molecular orbitals (MOs) are expanded in a plane-wave (PW) basis, while unoccupied MOs are derived primarily from localized atomic basis functions. The method accelerates spectral convergence when compared to fully PW-based simulations, with a $2-3$ fold reduction in the number of unoccupied MOs entering the Casida equation. The mixed-basis is placed on a common real-space grid, enabling our previously developed deterministic/sparse-stochastic evaluation of the exact exchange operator (DOI: 10.1021/acs.jctc.3c00987). This chemically intuitive and computationally efficient approach is validated across various molecular systems, including π-conjugated polymethine dyes, aromatic hydrocarbons, and a chlorophyll monomer.

I. INTRODUCTION

Time-dependent density functional theory (TDDFT) is a widely used method for the excited-state properties of molecules, known for possessing a remarkable balance between accuracy and computational efficiency. An extension of ground-state DFT, TDDFT is built upon the Runge-Gross theorem which reduces the time evolution of the many-body electronic wavefunction to the independent propagation of single-particle molecular orbitals (MOs). [1] Since its inception, TDDFT has been used in predicting both linear and nonlinear optical response, photoelectron spectra, and optoelectronic properties in general.[2–13] Modern implementations of TDDFT employ hybrid functionals that incorporate a fraction of Fock exchange to the exchange-correlation (XC) potential. Inclusion of exact exchange provides a better description of delocalized excited states, such as $\pi \rightarrow \pi^*$ transitions, charge-transfer excitations, and excitations in systems with pronounced excitonic effects.[14–20]

Going beyond the local density and generalized gradient approximations (LDA/GGA) [21, 22] offers improved accuracy but adds to the computational cost with the need to evaluate the exchange integrals. In previous work, we introduced a mixed deterministic/sparse-stochastic exchange approach that reduces the scaling of both hybrid DFT and linear-response TDDFT within a plane-wave (PW) representation.[23, 24] This method splits the exchange interaction kernel, $u(k)$, into low- and high-k components (where k denotes a reciprocal lattice vector):

$$\begin{aligned} u(k) = &\sum_{k_{\text{low}}} |k_{\text{low}}\rangle u(k_{\text{low}}) \langle k_{\text{low}}| \\ &+ \sum_{k_{\text{high}}} \sqrt{u(k_{\text{high}})} |k_{\text{high}}\rangle \langle k_{\text{high}}| \sqrt{u(k_{\text{high}})}. \end{aligned} \tag{1}$$

The low-k components are treated exactly while the high-k terms are represented by short (sparse) random vectors that uniformly sample the high-k space. The cutoff momentum, k_{cut}, that separates the low- and high-k spaces is a convergence parameter. The size of the stochastic basis sampling the high-k space is system-size independent, enabling large-scale hybrid TDDFT of molecular complexes with thousands of valence electrons.

In previous sparse-stochastic hybrid TDDFT calculations [24], we found that many unoccupied MOs (roughly three to four times the number of occupied states) are required to obtain a converged absorption spectrum. This issue of convergence is well-known and inherent to the use of a PW basis-set. [25, 26] In this work, we resolve this issue by implementing a mixed plane-wave/atomic-orbital (PW/AO) basis-set representation for the MOs. The integration of mixed basis sets, combining PWs and AOs, is very useful in computational chemistry and materials science.[27–32] For example, Samsonidze et al. demonstrated that unoccupied orbitals in GW calculations could be replaced with simple approximate physical orbitals, where Gaussian orbitals are used for resonant and continuum states.[33] Similarly, works conducted by Booth et al. and Sun et al. focus on Gaussian and PW hybrid representations alongside density fitting techniques.[25, 26]

We now turn to the primary focus of this article: how to reduce the number of unoccupied states entering the Casida equation through a mixed basis-set representation. Below, we present a PW/AO mixed-basis approach and its TDDFT applications on π-conjugated flavylium (Flav-9) and indocyanine green (ICG-7) dyes, curved aromatic corannulene ($C_{20}H_{10}$), as well as a monomer chlorophyll a (Chla) complex.

II. METHODOLOGY

Here we are interested in the optical absorption spectra of molecules using a mixed PW/AO basis-set representation for the MOs. In Section A, an iterative Chebyshev approach for efficiently calculating spectra is presented. In Section B, the mixing of PW and AO bases is outlined, and in Section C we show an orthonormaliza-

* dxn@ucla.edu

tion procedure for the combined basis-set MOs. Finally, in Section D we provide metrics for convergence of the TDDFT spectra.

A. Iterative approach for optical absorption spectra

Excitation energies are obtained by solving the Casida equation [2]:

$$\mathcal{L}\begin{pmatrix} f^+ \\ f^- \end{pmatrix} = \omega \begin{pmatrix} 1 & 0 \\ 0 & -1 \end{pmatrix} \begin{pmatrix} f^+ \\ f^- \end{pmatrix}, \tag{2}$$

where the Liouvillian is

$$\mathcal{L} = \begin{pmatrix} A & B \\ -B & -A \end{pmatrix}, \tag{3}$$

with f^+ and f^- transition eigenvectors corresponding to excitations and de-excitations, respectively. For single-particle spin-singlet excitations, the A and B matrices read (assuming real-valued MOs throughout):

$$\begin{aligned} A_{ia,jb} = (\varepsilon_a - \varepsilon_i)\delta_{ij}\delta_{ab} + 2(ia|jb) \\ + (ia|f_{\mathrm{XC}}|jb) - (\phi_a\phi_b|u|\phi_i\phi_j), \end{aligned} \tag{4}$$

$$B_{ia,bj} = 2(ia|bj) + (ia|f_{\mathrm{XC}}|bj) - (\phi_a\phi_j|u|\phi_i\phi_b), \tag{5}$$

where $\phi_{i,j,\ldots}$ denote occupied (valence) generalized Kohn-Sham (GKS) MOs with associated energies $\varepsilon_{i,j,\ldots}$ and $\phi_{a,b,\ldots}$ unoccupied (conduction) GKS MOs with energies $\varepsilon_{a,b,\ldots}$.

The Hartree integrals are:

$$(ia|jb) = \int dr\, dr'\, \phi_i(r)\phi_a(r)|r-r'|^{-1}\phi_j(r')\phi_b(r'). \tag{6}$$

The matrix elements of the XC kernel, f_{XC}, are evaluated to first-order within an adiabatic LDA scheme. [34] The exchange integrals are calculated under a kernel u that is split to short- and long-range parts in real space [14, 35]:

$$\begin{aligned} u(|r-r'|) = \frac{1-(\alpha+\beta\cdot\mathrm{erf}(\gamma|r-r'|))}{|r-r'|} \\ + \frac{\alpha+\beta\cdot\mathrm{erf}(\gamma|r-r'|)}{|r-r'|}. \end{aligned} \tag{7}$$

Rather than direct diagonalization of Eq. (3), we use an iterative Chebyshev polynomial expansion approach to access the eigenvalues of $\mathcal{L}$, as in Refs. [24, 36, 37]. The absorption spectrum is calculated as:

$$A(\omega) \propto \omega\langle\chi|\delta(\mathcal{L}-\omega)|\chi\rangle, \tag{8}$$

where

$$|\chi\rangle = \begin{pmatrix} \chi^+_{ia} \\ \chi^-_{ia} \end{pmatrix} = \begin{pmatrix} +\langle\phi_a|\hat{r}|\phi_i\rangle \\ -\langle\phi_a|\hat{r}|\phi_i\rangle \end{pmatrix}, \tag{9}$$

is a single exciton vector corresponding to a field polarization in the $\hat{r}$ direction. The Gaussian-broadened delta function is expanded in terms of Chebyshev polynomials:

$$\delta(\mathcal{L}-\omega) = \sum_{n=0}^{N_{\mathrm{Chebyshev}}} c_n(\omega)T_n(\tilde{\mathcal{L}}), \tag{10}$$

where T_n is the n'th-order Chebyshev polynomial and $\tilde{\mathcal{L}}$ is a scaled Liouvillian with eigenvalues between -1 and 1.[37, 38] $A(\omega)$ is therefore calculated from the Chebyshev moments,

$$A(\omega) = \frac{4\pi\omega}{c}\sum_{n=0}^{N_{\mathrm{Chebyshev}}} c_n(\omega)\langle\tilde{\chi}|T_n(\tilde{\mathcal{L}})|\chi\rangle, \tag{11}$$

where $|\tilde{\chi}\rangle = \pm|\chi\rangle$ and for the coefficients, $c_n(\omega)$, simple smoothly decaying weights are used [38].

B. Mixed-basis MOs on a real-space grid

First, we perform two separate LDA-DFT calculations, one using a PW basis and the other with a localized AO basis. All vacuum molecular geometries are optimized in the ORCA 6.0 program at the B3LYP/def2-TZVPPD level of theory.[39, 40] The PW calculations are performed using an in-house DFT code with norm-conserving pseudopotentials (NCPPs) representing the core electrons. [41] The all-electron AO-basis calculations utilize the *PySCF* package.[42] The choice of basis is guided by benchmark calculations on the $C_{20}H_{10}$ molecule, where we compare the lowest-occupied MO (LUMO) - highest-occupied MO (HOMO) energy gaps obtained from LDA-DFT using various basis sets against a reference grid-based PW-LDA-DFT calculation. Among the tested basis-sets, aug-cc-pVDZ yields the smallest deviation from the PW result, as detailed in Appendix A.[43]

In the PW-LDA-DFT calculations, the molecule is centered on a uniform real-space grid with a spacing of $dx = dy = dz = 0.4$ Bohr and the Martyna-Tuckerman approach is used to minimize edge effects. [44]. The simulation grids include at least 6 Bohr of padding beyond the extent of the molecule in all directions. Both the PW- and AO-MOs are then evaluated on this same grid. By replacing all or a subset of the unoccupied PW-MOs with those obtained from the AO calculation, we construct a mixed-basis representation of the MOs (Fig. 1).

For static bandgaps we find that all PW-based unoccupied states can be replaced with a lesser number of AO-derived MOs and still reproduce the gaps of the fully-PW based calculations. However, a more careful selection of the virtual-space MOs is required for excited-state simulations. For sparse-stochastic hybrid TDDFT calculations, we observe that retaining every fourth unoccupied MO from the PW basis while replacing the rest with AO-derived orbitals provides the best agreement with the first

excitation energies, i.e., absorption onset, obtained from fully PW-TDDFT. Specifically, the AO basis sets tend to overly localize, particularly in the virtual space, often resulting in a basis-set-induced blueshift. By retaining approximately 25% of the PW unoccupied MOs, we mitigate this shift and recover excitation energies consistent with fully PW-based calculations. To ensure a consistent set of MOs, we apply this same mixing strategy in both the static DFT and excited-state TDDFT simulations.

Further, the mixing of an all-electron AO basis-set with an NCPP-PW approach results in lower HOMO energies in the PW-LDA-DFT calculations. To ensure energy alignment between the two frameworks, we apply a scissor-shift correction ($\Delta\varepsilon$), i.e., $\varepsilon_i^{PW} = \varepsilon_i^{AO} + \Delta\varepsilon$, where $\Delta\varepsilon$ is determined from the difference between the HOMO energies [33].

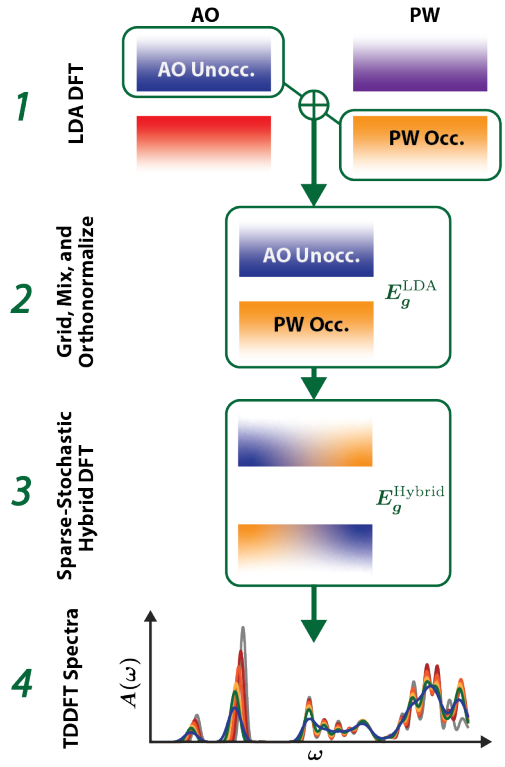

FIG. 1. Schematic representation of this work.

C. Orthonormalization

Subsequently, we perform an overall orthonormalization of the mixed-basis MOs using QR decomposition by Householder transformation.[45, 46] This is done by decomposing the eigenvector matrix $\sqrt{dV}C$, where the columns of C are non-orthogonal mixed LDA-DFT MOs and dV is the volume element, into an orthonormal matrix Q and an upper triangular matrix R. The columns of Q correspond to the orthonormalized MOs on the grid. While other orthonormalization techniques, such as Gram-Schmidt or Löwdin transformation with singular value decomposition (SVD),[47–51] are also applicable, we find the QR method via Householder transformation to be the most efficient. A Frobenius norm error analysis comparing different orthonormalization techniques is shown in Appendix B.

D. TDDFT Spectra and Spectral Convergence

With orthonormalized mixed-basis LDA MOs, we proceed with a sparse-stochastic hybrid DFT calculation using the CAM-LDA0 ($\alpha = 0.19, \beta = 0.46, \gamma = 0.33$ Bohr^{-1}).[17, 23, 24] This calculation updates the LDA-DFT Hamiltonian to include parametrized exact-exchange within a GKS-DFT framework. The hybrid exchange matrix elements are calculated using 1000 short stochastic fragments. For further details, see Ref. [23]. Subsequently, we perform sparse-stochastic hybrid TDDFT calculations with 1000 Chebyshev terms to compute the optical absorption spectra. All occupied valence electron MOs are included in the valence space ($N_v = N_{\mathrm{occ}}$), while in the TDDFT calculations the number of unoccupied MOs (N_c) is varied.

To quantify the convergence of optical spectra with respect to N_c, we define the deviation matrix D,

$$D_{ij} = \int |\tilde{A}_i(\omega) - \tilde{A}_j(\omega)|\, d\omega, \tag{12}$$

where $\tilde{A}(\omega)$ is the area-normalized absorption spectrum, $A(\omega)$, i.e., $\tilde{A}(\omega) = A(\omega)/\int A(\omega)\, d\omega$. Consequently, D_{ij} ranges between 0 (perfectly identical spectra) and 2 (completely different spectra). We further define two averaged quantities δ and $\bar{\delta}$,

$$\delta = \frac{1}{N-1} \sum_{i=1}^{N-1} D_{i,i+1}, \tag{13}$$

$$\bar{\delta} = \frac{2}{N(N-1)} \sum_{i<j} D_{ij}, \tag{14}$$

where N denotes the total number of spectra, each corresponding to a different value of N_c included in the TDDFT calculation. The quantity δ measures the average deviation between successive spectra, while $\bar{\delta}$ captures the average deviation over all pairs.

III. RESULTS AND DISCUSSION

Fig. 2 presents an orbital analysis of $C_{20}H_{10}$ to highlight the key similarities and differences between mixed-basis and pure PW MOs. Near the Fermi level, MOs such as the HOMO and LUMO exhibit comparable spatial density distributions and MO energies across both representations. However, for high-energy unoccupied states, the mixed-basis MOs differ substantially from their PW

counterparts. For example, as illustrated in Fig. 2(a), the LUMO+90 orbital in $C_{20}H_{10}$ exhibits more spatially contracted density in the mixed basis due to the AO component, leading to a higher orbital energy. In contrast, the same MO in the pure PW basis is more delocalized and energetically lower.

The MO energies for unoccupied states derived from the PW and AO bases (after aligning the HOMO energies) are shown in Fig. 2(b). As is well known, AO-basis MOs tend to be more spatially localized at higher energies compared to their PW counterparts. This increased localization leads to stronger electron–electron repulsion, and consequently, higher MO energies. This trend is also evident from the overlap matrix between the two sets of orbitals, defined as $S_{ij} = \langle \phi_i^{AO} | \phi_j^{PW} \rangle$, shown in Fig. 2(c). At higher energies, the spatial overlap between AO and PW MOs becomes noticeably smaller, reflecting their increasing dissimilarity.

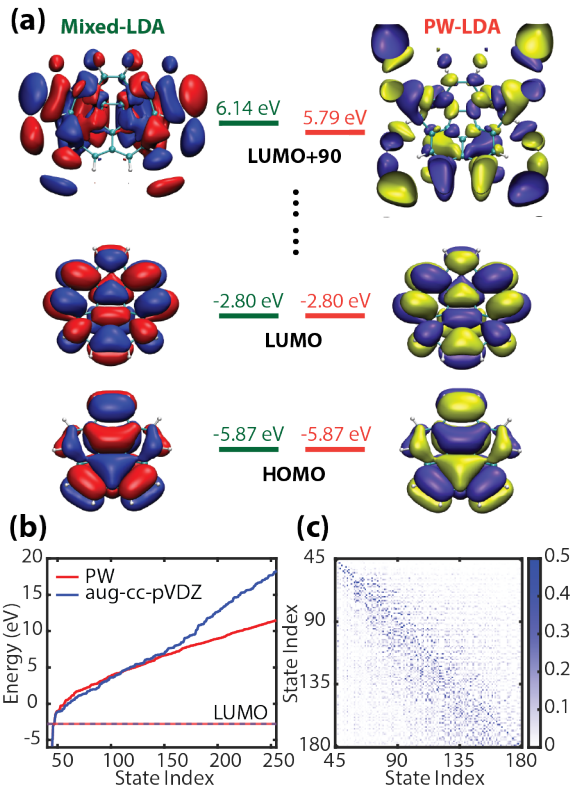

FIG. 2. **(a)** HOMO, LUMO, and LUMO+90 densities and energies for $C_{20}H_{10}$ calculated at the LDA level with the mixed PW/AO@aug-cc-pVDZ basis (left) and pure PW basis (right). **(b)** MO energy comparison for $C_{20}H_{10}$ for unoccupied states between PW and AO@aug-cc-pVDZ basis at LDA level (HOMO energies have been aligned with a rigid energy-shift of $\Delta\varepsilon = -1.24$ eV). **(c)** Overlap intensity between unoccupied LDA MOs from PW and AO@aug-cc-pVDZ basis for $C_{20}H_{10}$.

System	PW-LDA	AO-LDA	PW-Hybrid	Mixed-Hybrid
$C_{20}H_{10}$	3.05	3.07	6.71	6.70
Chla	1.42	1.43	3.90	3.89
ICG-7	1.19	1.20	3.89	3.89
Flav-9	0.90	0.90	3.05	3.04

TABLE I. Static LUMO-HOMO gaps (in eV) for four test systems from PW-LDA-DFT, AO@aug-cc-pVDZ LDA-DFT, PW- and mixed PW/AO- sparse-stochastic hybrid-DFT with CAM-LDA0.

Static LDA-DFT and sparse-stochastic hybrid-DFT LUMO–HOMO gaps are presented in Table I. Both the initial PW-LDA-DFT and AO-LDA-DFT calculations yield nearly identical results, with differences under 0.02 eV across all test systems. This agreement is maintained at the hybrid-DFT stage. The consistency of ground-state properties establishes a robust foundation for subsequent excited-state calculations using the mixed-basis approach.

Fig. 3 shows sparse-stochastic hybrid TDDFT@CAM-LDA0 spectra for $C_{20}H_{10}$ with $N_v = N_{\rm occ} = 45$ calculated with N_c values ranging from 45 to 160, using the mixed PW/AO basis (Fig. 3(a)) and the pure PW basis (Fig. 3(b)). Fig. 3(c) shows the molecular structure, and Fig. 3(d) displays the spectral deviation matrix D comparing mixed PW/AO (left) and PW (right) bases. Fig. 4 presents similar data for Chla, with $N_v = 116$ and $N_c = 174 - 464$; Fig. 5 reports the results for ICG-7, using $N_v = 115$ and $N_c = 173 - 460$; finally, Fig. 6 shows results for Flav-9, using $N_v = 116$ and $N_c = 174 - 464$, with the same panel arrangements.

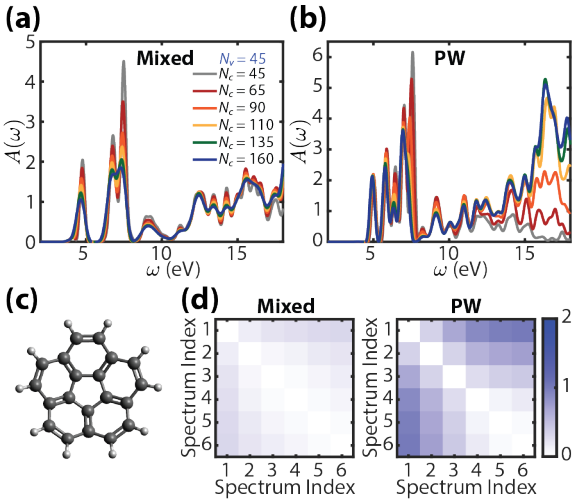

FIG. 3. $\mathbf{C_{20}H_{10}}$: sparse-stochastic hybrid TDDFT@CAM-LDA0 spectra calculated with different N_c values via **(a)** mixed PW/AO and **(b)** PW basis, $N_v = N_{\rm occ} = 45$ is used for all calculations. **(c)** Molecular structure **(d)** the spectral deviation matrix D from mixed PW/AO (left) and PW (right) basis.

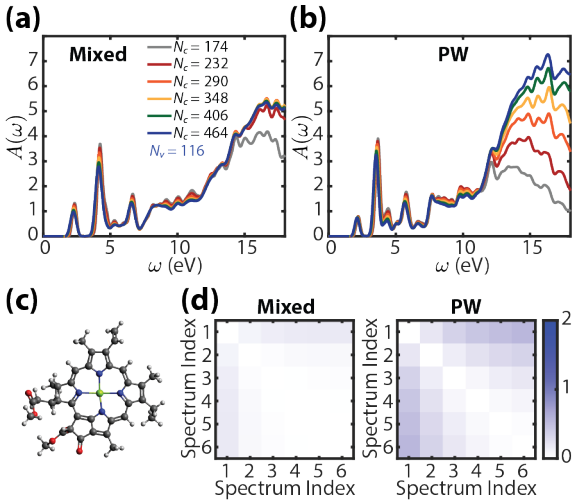

FIG. 4. **Chla**: sparse-stochastic hybrid TDDFT@CAM-LDA0 spectra calculated with different N_c values via **(a)** mixed PW/AO and **(b)** PW basis, $N_v = 116$ is used for all calculations. **(c)** Molecular structure **(d)** the spectral deviation matrix D from mixed PW/AO (left) and PW (right) basis.

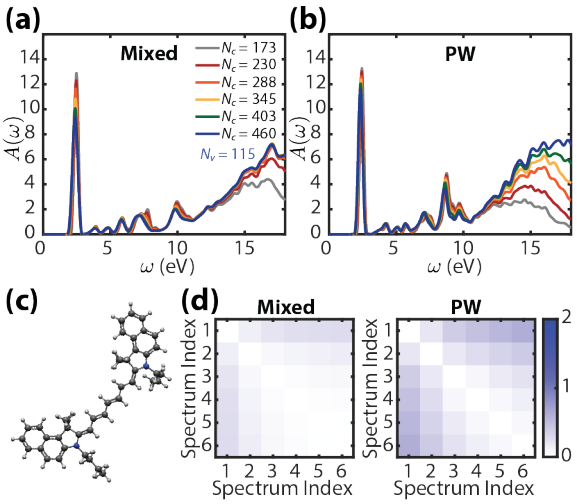

FIG. 5. **ICG-7**: sparse-stochastic hybrid TDDFT@CAM-LDA0 spectra calculated with different N_c values via **(a)** mixed PW/AO and **(b)** PW basis, $N_v = 115$ is used for all calculations. **(c)** Molecular structure **(d)** the spectral deviation matrix D from mixed PW/AO (left) and PW (right) basis.

Notably, the mixed-basis approach exhibits significantly improved convergence across all four test systems, particularly in the high-energy regions of the spectra. This improvement arises because the more contracted AO basis renders the high-energy MOs more localized, and consequently, the corresponding transitions become more spatially confined. The spectral deviation matrices, presented in Panel (d) of Figs. 3 through 6, provide additional insights into spectral behavior during the convergence process. The spectrum index, i, ranges from 1 to 6, where each i labels a different value of N_c; 1 refers to the smallest N_c used and 6 labels the largest. These matrices consistently show smaller off-diagonal components for mixed-basis calculations compared to pure PW results, indicating more stable and systematic convergence as N_c increases.

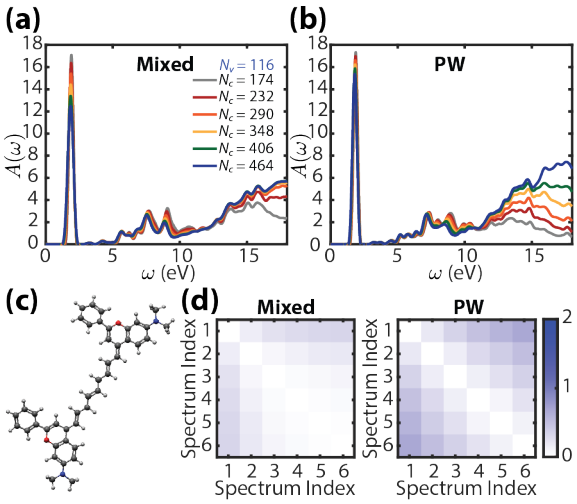

FIG. 6. **Flav-9**: sparse-stochastic hybrid TDDFT@CAM-LDA0 spectra calculated with different N_c values via **(a)** mixed PW/AO and **(b)** PW basis, $N_v = 116$ is used for all calculations. **(c)** Molecular structure **(d)** the spectral deviation matrix D from mixed PW/AO (left) and PW (right) basis.

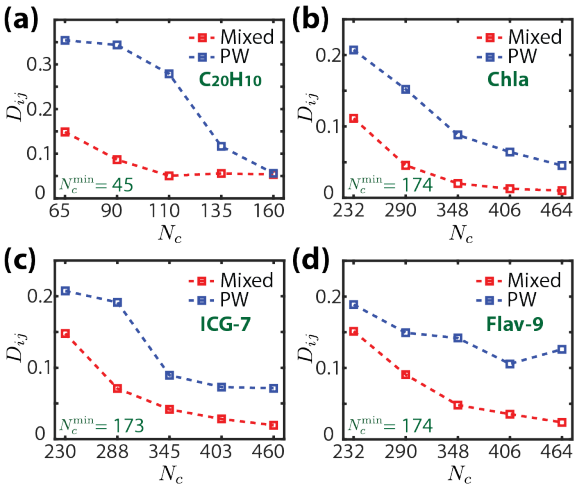

FIG. 7. Deviation between consecutive pairs of spectra for **(a)** $C_{20}H_{10}$, **(b)** Chla, **(c)** ICG-7, and **(d)** Flav-9, comparing the mixed- and PW-basis approaches. Each data point represents the deviation between spectra at a given N_c (shown on the x-axis) and the preceding N_c value. The left-most point corresponds to the deviation between the smallest N_c used ($N_c^{\min}$, labeled in each plot) and its immediate next value.

To better understand the trend in spectral conver-

gence, we plot the deviation between consecutive spectral pairs, $D_{i,i+1}$, in Fig. 7. For $C_{20}H_{10}$, $N_c^{Mixed} = 110 = 2.5N_v$ achieves equivalent convergence to $N_c^{PW} = 160 = 3.6N_v$ (Fig. 7(a)). For Chla, $N_c^{Mixed} = 290 = 2.5N_v$ reproduces $N_c^{PW} = 494 = 4.3N_v$ (Fig. 7(b)). The ICG-7 system follows this trend, where $N_c^{Mixed} = 288 = 2.5N_v$ delivers comparable accuracy to $N_c^{PW} = 460 = 4N_v$ (Fig. 7(c)). Finally, Flav-9 requires only $N_c^{Mixed} = 290 = 2.5N_v$ to reach the convergence level of $N_c^{PW} = 464 = 4N_v$ (Fig. 7(d)).

The overall convergence metrics δ and $\bar{\delta}$ are summarized in Table II. The mixed-basis calculations show significantly lower δ and $\bar{\delta}$ values compared to their PW counterparts. Specifically, we observe a $2-3$ fold reduction in the values for δ and $\bar{\delta}$ using the mixed-based representation of the MOs relative to a purely PW-based representation. This enhanced performance originates from the more compact and chemically intuitive representation of high-energy conduction states in the AO basis, which effectively reduces the number of conduction states (N_c) required for achieving spectral convergence.

System	δ (Mixed)	δ (PW)	$\bar{\delta}$ (Mixed)	$\bar{\delta}$ (PW)
$C_{20}H_{10}$	0.08	0.23	0.16	0.51
Chla	0.04	0.11	0.08	0.25
ICG-7	0.06	0.13	0.13	0.29
Flav-9	0.07	0.14	0.15	0.32

TABLE II. The average deviation between successive spectra (δ) and the average deviation over all pairs ($\bar{\delta}$) via PW and mixed-basis for four test systems with six tested values of N_c, ranging from $N_c = N_v$ to $N_c = 4N_v$.

However, our analysis also reveals an important subtlety regarding the first excitation energy, i.e., the optical gap. While the overall spectral shapes show excellent agreement between the PW and mixed-basis calculations, we consistently observe a small (~ 0.08 eV) but systematic blueshift in the optical gaps.[52, 53] This observation suggests that, although the mixed basis is highly effective for describing higher-energy excitations and provides significantly faster spectral convergence, special care is required when precise determination of the optical gap is needed.

IV. CONCLUSION

This study demonstrates the advantages of combining PW and AO basis sets within the sparse-stochastic hybrid TDDFT framework, offering a balanced approach that maintains accuracy while improving computational efficiency. The mixed-basis method, leveraging PW-derived occupied MOs and carefully selected AO-derived unoccupied MOs, achieves results with superior spectral convergence with respect to the number of conduction states. Our analysis confirms excellent agreement for ground-state properties in sparse-stochastic hybrid DFT calculations, where the LUMO-HOMO gap deviations between the PW and mixed-basis calculations are below 0.02 eV. The sparse-stochastic hybrid TDDFT spectral calculations show that the localized nature of AOs enhances convergence for high-energy excitations and offers an overall $2-3$ folds faster convergence.

Looking ahead, this work opens several promising avenues for development, including optimized mixing ratios of PW- and AO-derived MOs in the unoccupied space, extension to periodic boundary conditions, and integration with fragment-based methods for large-scale simulations.

ACKNOWLEDGMENTS

This work is supported by the National Science Foundation (NSF) under Grant No. CHE-2245253. Computational resources for simulations were provided by both the Expanse cluster at the San Diego Supercomputer Center through allocation CHE-230099 under the Advanced Cyberinfrastructure Coordination Ecosystem: Services & Support (ACCESS) program and the Hoffman2 Shared Cluster provided by UCLA Office of Advanced Research Computing's Research Technology Group.

APPENDIX A: BASIS-SET BENCHMARKING

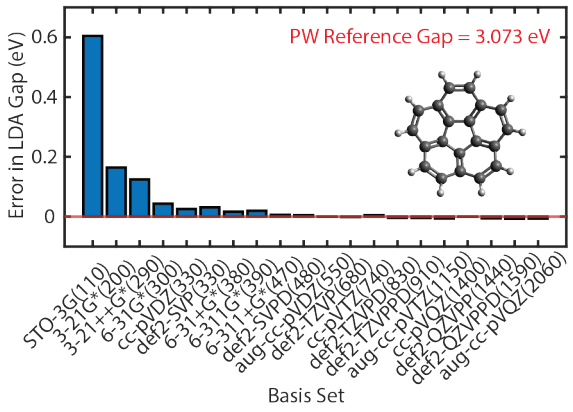

FIG. 8. LUMO-HOMO LDA gap differences (compared to the PW-LDA result) in eV calculated for $C_{20}H_{10}$, using various AO basis sets. The numbers in parentheses indicate the total number of basis functions used. The minimum deviation AO set is aug-cc-pVDZ with 550 total basis functions, where the gap difference between AO and PW is -6.05×10^{-4} eV.

Localized AO basis sets vary widely in their composition and completeness, ranging from minimal sets like STO-3G to highly extensive ones such as aug-cc-pVQZ. In principle, as an AO basis set becomes more complete, its results should asymptotically approach those

of PW calculations. However, this increased completeness comes at a significantly higher computational cost. To identify an optimal AO basis set for the mixed-basis scheme, we benchmark several AO basis sets by performing LDA-DFT calculations and comparing the resulting LUMO-HOMO gaps against those from a reference PW LDA-DFT calculation. The error is defined as the difference between AO and the reference PW gaps. All benchmarks are conducted on the $C_{20}H_{10}$ (Fig. 8).

Since our calculations employ real-space grids, we require basis functions with smooth spatial decay to maintain numerical stability in integrations.[54, 55] The aug-cc-pVDZ basis set satisfies this need by avoiding excessively sharp Gaussian exponents (ζ): carbon's tightest exponent in aug-cc-pVDZ has $\zeta \sim 8 \times 10^3$ Bohr^{-2} is far smoother than in sharper sets like 6-31G* with $\zeta \sim 2 \times 10^4$ Bohr^{-2} or STO-3G with $\zeta \sim 7 \times 10^4$ Bohr^{-2}.[56, 57] This careful balance prevents the grid artifacts that would arise from extreme exponents while maintaining accuracy for both core and valence electrons.

APPENDIX B: COMPARISON OF ORTHONORMALIZATION TECHNIQUES

The orthonormality condition on the numerical grid is checked via the Frobenius error

$$\|I - S\|_2 = \sqrt{\sum_{i,j} |(I-S)_{ij}|^2}, \tag{15}$$

where I is the identity matrix and S is the overlap matrix of the orthonormalized MOs (Table III).

	Householder	Gram-Schmidt	Löwdin
$C_{20}H_{10}$	1.41×10^{-14}	1.63×10^{-14}	2.05×10^{-13}
Chla	4.10×10^{-14}	3.96×10^{-14}	2.06×10^{-13}
ICG-7	4.24×10^{-14}	4.24×10^{-14}	4.64×10^{-13}
Flav-9	4.72×10^{-14}	4.58×10^{-14}	3.64×10^{-13}

TABLE III. $\|I - S\|_2$ Frobenius error using different orthonormalization procedures.

To identify the optimal procedure here, we benchmark results from three different approaches: Löwdin orthonormalization, Gram-Schmidt, and Householder transformation. Once the cost of making S is included, all methods scale as $\mathcal{O}(N_g M^2)$, where $M = N_v + N_c$ is the total number of MOs and N_g is the number of grid-points. Although Gram-Schmidt offers slightly better accuracy for larger molecules, we use the Householder transformation due to its availability as highly optimized low-level code in Python packages.

APPENDIX C: COMPUTATIONAL PARAMETERS

General computational parameters are tabulated in Table IV.

System	N_x	N_y	N_z	dx	N_v	N_c	$N_{k_{\text{low}}}$
$C_{20}H_{10}$	70	70	40	0.4	45	45 − 160	201
Chla	106	96	80	0.4	116	174 − 464	867
ICG-7	130	100	80	0.4	115	173 − 460	1127
Flav-9	156	100	70	0.4	116	174 − 464	1195

TABLE IV. Computational parameters for the four test systems: grid extents, isotropic grid-spacing of $dx = dy = dz = 0.4$ Bohr is used for all systems, N_v values, and N_c ranges used for sparse-stochastic hybrid DFT and TDDFT calculations. $N_{k_{\text{low}}}$ is the number of deterministically treated long-wavelength terms in the exchange kernel $u(k)$. The high-k space is represented with 1000 sparse-stochastic vectors, details are provided in Refs. [23, 24].

DATA AVAILABILITY

The data that supports the findings of this study are available within the article and appendixes. Additional data that support the findings of this study are available from the corresponding author upon request.

[1] E. Runge and E. K. U. Gross, Phys. Rev. Lett. **52**, 997 (1984).
[2] M. E. Casida, World Sci. **1**, 155 (1995).
[3] C. Jamorski, M. E. Casida, and D. R. Salahub, J. Chem. Phys. **104**, 5134 (1996).
[4] K. Yabana and G. Bertsch, Z. Phys. D: At., Mol. Clusters **42**, 219 (1997).
[5] K. Yabana and G. F. Bertsch, Int. J. Quantum Chem. **75**, 55 (1999).
[6] K. Lopata, B. E. Van Kuiken, M. Khalil, and N. Govind, J. Chem. Theory Comput. **8**, 3284 (2012).
[7] S. DeBeer George, T. Petrenko, and F. Neese, Inorg. Chim. Acta **361**, 965 (2008).
[8] J. Lermé, B. Palpant, B. Prével, E. Cottancin, M. Pellarin, M. Treilleux, J. Vialle, A. Perez, and M. Broyer, Eur. Phys. J. D **4**, 95 (1998).
[9] X. Qian, J. Li, X. Lin, and S. Yip, Phys. Rev. B: Condens. Matter Mater. Phys. **73**, 035408 (2006).
[10] R. Baer and D. Neuhauser, Int. J. Quantum Chem. **91**, 524 (2003).
[11] R. Baer and R. Gould, J. Chem. Phys. **114**, 3385 (2001).
[12] T. Zelovich, L. Kronik, and O. Hod, J. Chem. Theory Comput. **10**, 2927 (2014).

[13] F. Ding, B. E. Van Kuiken, B. E. Eichinger, and X. Li, J. Chem. Phys. **138**, 064104 (2013).
[14] A. D. Becke, J. Chem. Phys. **98**, 5648 (1993).
[15] R. Baer, E. Livshits, and U. Salzner, Annu. Rev. Phys. Chem. **61**, 85 (2010).
[16] T. Leininger, H. Stoll, H.-J. Werner, and A. Savin, Chem. Phys. Lett. **275**, 151 (1997).
[17] T. Yanai, D. P. Tew, and N. C. Handy, Chemical Physics Letters **393**, 51–57 (2004).
[18] A. Karolewski, T. Stein, R. Baer, and S. Kümmel, J. Chem. Phys. **134**, 151101 (2011).
[19] L. Kronik, T. Stein, S. Refaely-Abramson, and R. Baer, J. Chem. Theory Comput. **8**, 1515 (2012).
[20] V. Vlček, R. Baer, and D. Neuhauser, J. Chem. Phys. **150**, 184118 (2019).
[21] J. P. Perdew and Y. Wang, Phys. Rev. B **45**, 13244 (1992).
[22] J. P. Perdew, K. Burke, and M. Ernzerhof, Physical Review Letters **77**, 3865 (1996).
[23] N. C. Bradbury, T. Allen, M. Nguyen, and D. Neuhauser, Journal of Chemical Theory and Computation **19**, 9239–9247 (2023).
[24] M. Sereda, T. Allen, N. C. Bradbury, K. Z. Ibrahim, and D. Neuhauser, Journal of Chemical Theory and Computation **20**, 4196–4204 (2024).
[25] G. H. Booth, T. Tsatsoulis, G. K. L. Chan, and A. Grüneis, Journal of Chemical Physics **145** (2016), 10.1063/1.4961301.
[26] Q. Sun, T. C. Berkelbach, J. D. McClain, and G. K. L. Chan, Journal of Chemical Physics **147** (2017), 10.1063/1.4998644.
[27] R. Colle, A. Fortunell, and S. Simonucci, IL NUOVO CIMENTO **9**, 969 (1987).
[28] R. N. Euwema, Physical Review B **4**, 4332 (1971).
[29] M. D. Fabian, E. Rabani, and R. Baer, Chemical Physics Letters **865** (2025), 10.1016/j.cplett.2025.141912.
[30] P. Cársky, M. Polášek, and J. Heyrovsk´yheyrovsk´y, JOURNAL OF COMPUTATIONAL PHYSICS **143**, 266 (1998).
[31] J. Liu and J. Herbert, J. Chem. Phys. **143**, 034106 (2015).
[32] H.-Y. Ko, B. Santra, and R. A. DiStasio Jr, J. Chem. Theory Comput. **17**, 7789 (2021).
[33] G. Samsonidze, M. Jain, J. Deslippe, M. L. Cohen, and S. G. Louie, Physical Review Letters **107** (2011), 10.1103/PhysRevLett.107.186404.
[34] S. Baroni, P. Giannozzi, and A. Testa, Phys. Rev. Lett. **58**, 1861 (1987).
[35] T. Leininger, H. Stoll, H.-J. Werner, and A. Savin, Chemical Physics Letters **275**, 151 (1997).
[36] N. C. Bradbury, M. Nguyen, J. R. Caram, and D. Neuhauser, The Journal of Chemical Physics **157**, 031104 (2022).
[37] N. C. Bradbury, T. Allen, M. Nguyen, K. Z. Ibrahim, and D. Neuhauser, The Journal of Chemical Physics **158**, 154104 (2023).
[38] A. Weiße, G. Wellein, A. Alvermann, and H. Fehske, Rev. Mod. Phys. **78**, 275 (2006).
[39] F. Neese, F. Wennmohs, U. Becker, and C. Riplinger, Journal of Chemical Physics **152** (2020), 10.1063/5.0004608.
[40] F. Neese, WIREs Computational Molecular Science **12**, e1606 (2022).
[41] N. Troullier and J. L. Martins, Phys. Rev. B **43**, 1993 (1991).
[42] Q. Sun, T. C. Berkelbach, N. S. Blunt, G. H. Booth, S. Guo, Z. Li, J. Liu, J. D. McClain, E. R. Sayfutyarova, S. Sharma, S. Wouters, and G. K. L. Chan, Wiley Interdisciplinary Reviews: Computational Molecular Science **8** (2018), 10.1002/wcms.1340.
[43] T. H. Dunning, K. A. Peterson, and A. K. Wilson, J. Chem. Phys. **114**, 9244 (2001), covers extensions and optimizations of cc-pVXZ/aug-cc-pVXZ.
[44] G. J. Martyna and M. E. Tuckerman, The Journal of Chemical Physics **110**, 2810 (1999).
[45] G. H. Golub and P. Businger, Numer. Math. **7**, 269 (1965).
[46] W. H. Press, S. A. Teukolsky, W. T. Vetterling, and B. P. Flannery, *Numerical Recipes: The Art of Scientific Computing*, 3rd ed. (Cambridge University Press, 2007) Chap. 2.10, householder QR decomposition in computational physics.
[47] A. Szabo and N. S. Ostlund, *Modern Quantum Chemistry: Introduction to Advanced Electronic Structure Theory* (Dover, 1996) Chap. 1.4, gram-Schmidt in quantum chemistry basis sets.
[48] J. W. Daniel, W. B. Gragg, L. Kaufman, and G. W. Stewart, Math. Comp. **30**, 772 (1976).
[49] G. H. Golub and C. Reinsch, Numer. Math. **14**, 403 (1970).
[50] P.-O. Löwdin, J. Chem. Phys. **18**, 365 (1950).
[51] D. R. Bowler and T. Miyazaki, Rep. Prog. Phys. **75**, 036503 (2012), covers SVD in DFT applications.
[52] F. Bruneval and X. Gonze, Phys. Rev. B **78**, 085125 (2008).
[53] D. Rocca, R. Gebauer, Y. Saad, and S. Baroni, The Journal of Chemical Physics **128**, 154105 (2008).
[54] A. D. Becke, The Journal of Chemical Physics **88**, 2547 (1988), https://pubs.aip.org/aip/jcp/article-pdf/88/4/2547/18968948/2547_1_online.pdf.
[55] A. D. Becke, Phys. Rev. A **38**, 3098 (1988).
[56] J. Dunning, Thom H., The Journal of Chemical Physics **90**, 1007 (1989), https://pubs.aip.org/aip/jcp/article-pdf/90/2/1007/18974738/1007_1_online.pdf.
[57] B. P. Pritchard, D. Altarawy, B. Didier, T. D. Gibson, and T. L. Windus, Journal of Chemical Information and Modeling **59**, 4814 (2019), pMID: 31600445, https://doi.org/10.1021/acs.jcim.9b00725.